

# Comparison of myelin sensitivity using model-based and model-free analysis of the water resonance line-shape in postmortem mouse brain

Scott Trinkle<sup>1</sup>, Gregg Wildenberg<sup>2</sup>, Narayanan Kasthuri<sup>2</sup>, Patrick La Rivière<sup>1</sup> Sean Foxley<sup>1</sup>

<sup>1</sup> Department of Radiology, University of Chicago, Chicago, IL, USA

<sup>2</sup> Department of Neurobiology, University of Chicago, Chicago, IL, USA

## Correspondence

Scott Trinkle, Department of Radiology, University of Chicago, 5841 South Maryland Avenue,  
MC2026, Chicago, IL, 60637  
Email: trinkle@uchicago.edu

## Abstract

**Purpose:** Dysmyelinating disorders lead to abnormalities in myelin structure that produce detectable effects in a magnetic resonance (MR) signal. To estimate the voxel-wise proportion of myelin, spectroscopic MR data are typically fit to simple compartmental models in the time domain. This work characterizes biases in these models by comparing high-resolution water spectra measured in postmortem fixed mouse brains with 3D echo-planar spectroscopic imaging (EPSI) to spectra predicted by time-domain models fit to the same data, specifically by comparing spectra from control and shiverer mice, a model for dysmyelination.

**Methods:** Perfusion-fixed, resected control ( $n = 5$ ) and shiverer ( $n = 4$ ) mouse brains were imaged using EPSI with 100  $\mu\text{m}$  isotropic resolution. The free induction decay (FID) was sampled every 2.74 ms over 192 echoes and Fourier transformed to produce water spectra with 1.9 Hz resolution. FIDs were also fit to two biophysical models and the resulting fits were converted to spectra with a Fourier transform. Spectral asymmetry was computed and compared before and after fitting the data to models.

**Results:** Spectra derived from both models underestimate the magnitude of asymmetric broadening observed in the raw data. Correlations between data- and model-derived asymmetries and estimated frequency shifts are weak, leading to a strong reduction in spectral sensitivity to myelin after fitting the data to models.

**Conclusion:** The results confirm and quantify biases in existing biophysical models and promote the further development of spectral analysis methods to benchmark new model-based approaches.

**Key words:** EPSI; biophysical models; myelin imaging; magnetic susceptibility; postmortem mouse brain; white matter

# 1 Introduction

Myelin is a lipid-rich substance produced by oligodendrocytes in the central nervous system that physically surrounds axons in order to improve the transmission of action potentials [1]. Its importance to the normal function of the human brain has been demonstrated through the symptoms of demyelination disorders such as multiple sclerosis, as well as through additional disorders related to defective myelin structure such as hypomyelination, dysmyelination, and myelinolysis [2].

Conventional clinical MRI approaches to the diagnosis of myelin disorders use combinations of  $T_1$ -weighted,  $T_2$ -weighted, and FLAIR acquisitions and have been shown to have poor specificity to myelin [3–5], prompting the development of approaches such as myelin water imaging [6, 7], which uses a multi-echo spin-echo sequence to estimate a myelin component within the  $T_2$  distribution. Recently, the use of a multi-gradient echo (MGE) sequence, also referred to as echo-planar spectroscopic imaging (EPSI), has emerged as an alternative to myelin water imaging [8–15]. EPSI measures a portion of the voxel-wise  $T_2^*$  decay curve, and results in faster scan times, a larger volume coverage, and a lower specific absorption rate than the sequences used for myelin water imaging [16].

To estimate myelin content and integrity from the EPSI signal, the free induction decay (FID) curves are fit to a biophysical model that typically assumes the white matter is composed of three distinct, nonexchanging water components: myelin water, intra-axonal water, and extracellular water, each with distinct  $T_2^*$  values and potential magnetic susceptibility-dependent frequency shifts [8, 11, 12, 16, 17]. These approaches rely on a simple underlying geometric model of white matter that uses nested, circular cylinders to describe axons [12, 18, 19]. A recent study [20] used biophysical models to simulate the MR signal arising from axons under different geometric models. It showed that as the axon geometry model becomes more realistic through the use of warped cylinders and segmented cross-sections from electron micrographs, the generated microscopic magnetic field becomes increasingly complex and the compartment-specific components of the resulting water spectra become much less pronounced and distinct, leading to a slightly asymmetric broadening around the main peak as opposed to discernible narrow peaks corresponding to each compartment. This suggests that quantitative microstructural imaging tasks that rely on these simple biophysical models might be biased by the models' assumed geometries.

Our previous work has demonstrated model-free sensitivity to myelin through direct analysis of the water resonance line-shape calculated from the fully-sampled FID. We have shown that a simple spectral asymmetry metric is sensitive to the presence of white matter as well as to the angle between the principal orientation of the constituent fibers and the main magnetic field ( $B_0$ ) [14]. We further identified myelin as a contributing source of this sensitivity through a comparison of data from both control and mutant "shiverer" ( $Mbp^{Shi}$ ) postmortem, fixed mouse brains [15]. Shiverer mice serve as a dysmyelination model due to a mutation that leads to the production of abnormal, thin, loosely-packed myelin sheaths [21], allowing for a quantification of the measurable differences in the water resonance line-shape attributable to differences in

myelination.

In this work, we extend our analysis of water spectra from control and shiverer mouse brains to explore the performance of two biophysical compartmental models published by Van Gelderen et al. [17] and Nam et al. [11]. We quantify the asymmetric broadening predicted after fitting the data to these models and compare it to the broadening measured directly in the data itself to show that biases in the models lead to compromised sensitivity to myelin.

## 2 Methods

### 2.1 Sample preparation

Procedures for the collection of the EPSI and diffusion MRI data used for this study have been published in a previous study [15] and are repeated here for completeness. All procedures performed on animals followed protocols approved by the Institutional Animal Care and Use Committee and were in compliance with the Animal Welfare Act and the National Institutes of Health Guide for the Care and Use of Laboratory Animals. Adult mice were deeply anesthetized with 60 mg/kg pentobarbital and sacrificed by intercardial perfusion with a solution (pH 7.4) of 0.1 M sodium cacodylate and heparin (15 units/ml). This was immediately followed by a solution of 2% paraformaldehyde, 2.5% glutaraldehyde, and 0.1 M sodium cacodylate (pH 7.4). Brains were carefully removed from the skulls and post-fixed in the same fixative overnight at 4°C. Brains were soaked in phosphate buffered saline (PBS) prior to imaging for at least 72 hours to remove fixative from the tissue.

### 2.2 MR imaging

Resected control ( $n = 5$ ) and shiverer ( $n = 4$ ) mouse brains were dried of excess PBS and placed in 10 ml Falcon tubes. Tubes were filled with Fluorinert (FC-3283, 3M Electronics) for susceptibility matching and to improve shimming.

Data were acquired at 9.4 T (20 cm internal diameter, horizontal bore, Bruker BioSpec Small Animal MR System, Bruker Biospin, Billerica, MA) using a 6 cm high performance gradient insert (maximum gradient strength: 1000 mT/m, Bruker Biospin) and a 35 mm internal diameter quadrature volume coil (Rapid MR International, Columbus, Ohio). Brains were aligned such that the anterior/posterior portion of the olfactory limb of the anterior commissure was approximately parallel to  $B_0$  and the hemispheric midline was parallel to the scanner YZ plane. This ensured consistency of position relative to  $B_0$  across samples.

Third-order shimming was iteratively performed over an ellipse that encompassed the entire brain, but did not extend beyond the boundaries of the Falcon tube/Fluorinert interface, using the Paravision mapshim protocol.  $B_0$  maps were produced by recording the voxel-wise frequency of the peak of the resonance, including additional sub-spectral resolution frequency produced by estimating the maximum peak amplitude

of the resonance, described below. This was consistent with previously reported work [13, 14] which described a high degree of field homogeneity across samples.

Diffusion MRI (dMRI) was performed using a conventional 3D spin-echo/Stejskal-Tanner diffusion-weighted sequence (TR = 600 ms, TE = 11.389 ms, b-value = 3000 s/mm<sup>2</sup>, δ = 3.09 ms, Δ = 6 ms, spatial resolution = 125 μm isotropic, number of b0s = 8, number of directions = 30, receiver bandwidth = 150 kHz, duration = 36h 28min 48s).

3D-EPSI data were acquired using a MGE sequence with an oscillating readout gradient train. Note that while the terms MGE and EPSI are synonymous, in the context of this paper, we will refer to MGE for data analysis in the temporal domain and EPSI for data analysis in the frequency domain. Sequence parameters were chosen so that the entire voxel-wise free induction decay was sampled to the noise floor with sufficiently high temporal resolution. This ensured that resultant spectra did not have FID truncation-related ringing artifacts, and that they had sufficient bandwidth, respectively (TR = 1000 ms, TE of first echo = 2.74 ms, echo spacing = 2.74 ms, number of echoes = 192, receiver bandwidth = 75 kHz, flip angle = 68°, 100 μm isotropic resolution, four averages, duration = 12 h). It is worth noting that scan times using this approach can be made more clinically relevant by acquiring 2D data with more modest spatial resolution and covering more targeted slabs of tissue. Previous work has shown *in vivo* human brain imaging performed with acquisition times on the order of 90 s with 1.5 × 1.5 × 4 mm<sup>3</sup> voxels over five slices [22, 23].

## 2.3 EPSI data processing

The following EPSI data processing and data analysis steps have also been reported elsewhere [14, 15] but are summarized here for completeness. Modifications reflecting differences in this work have been made.

EPSI data were processed and analyzed with IDL (ITT Visual Information Solutions, Boulder CO), Matlab (The MathWorks Inc., Natick, MA, 2012), and FSL (FMRIB Software Library, FMRIB, Oxford, UK). 3D multiple-gradient echo data were processed to produce voxel-wise water spectra. Each 4D complex array ( $k_x \times k_y \times k_z \times t$ ) was Fourier transformed in all dimensions to produce three spatial dimensions and one spectral dimension ( $x \times y \times z \times \nu$ ). For the complex spectrum,  $\nu$ , spectral ghosting was corrected at each point in space (x, y, z) [24]. The maximum peak magnitude was estimated in each voxel by applying the Fourier shift theorem to the complex data; the addition of a linear phase term in the temporal domain performs sub-spectral resolution shifts in the frequency domain allowing for the identification of the maximum signal magnitude for voxels in which the peak was located between Fourier components [25]. This process was alternately iterated with a zeroth-order phase correction to produce pure absorption spectra [26].

Water peak height (PH) images were constructed with image contrast produced by the maximum voxel-wise signal amplitude of the water spectrum [27]. This can be achieved by shifting the position of the maximum peak amplitude of the water resonance to the central Fourier component of the frequency axis. This step also serves to eliminate any relative background field information from each spectrum with little computational effort; this is analogous to implementing a background field removal technique, such as the

PDF [28] or the SHARP [29] filter, to  $T_2^*$ -weighted gradient echo data processed in the temporal domain.

The EPSI datasets contained a number of regions with signal drop-out resulting from the magnetic susceptibility mismatch between the tissue and bubbles stuck to the surface of the brain or trapped in the ventricles. To exclude these regions from downstream analysis, artifact masks were constructed for each dataset using the Atropos tissue segmentation algorithm in the ANTs [30] software package on the water peak-height images. First, brain masks were automatically generated using the bet protocol in FSL [31]. The algorithm was then initialized with a three-class K-means classification of the water peak-height images, with the classes representing white matter, gray matter, and joint CSF/artifact. Voxels in the CSF/artifact class were excluded from all further analysis. A sample image showing tissue classification and artifact filtering is shown in Supporting Information Figure S1.

## 2.4 Model fitting

Myelin imaging with MGE data has typically relied on the use of a three-compartment model for white matter, with separate  $T_2^*$  and frequency shifts stemming from axonal water, extracellular water, and myelin water. At its simplest, the time-dependent magnitude  $|S_i(t)|$  of the MGE signal at voxel  $i$  is modeled as a sum of exponentials for each compartment [8, 16]:

$$|S_i(t)| = A_{\text{my}}e^{-t/T_{2,\text{my}}^*} + A_{\text{ax}}e^{-t/T_{2,\text{ax}}^*} + A_{\text{ex}}e^{-t/T_{2,\text{ex}}^*}, \quad (1)$$

where  $A_{\text{my}}$ ,  $A_{\text{ax}}$ , and  $A_{\text{ex}}$  refer to the amplitudes of the myelin, axonal, and extracellular compartments in voxel  $i$ , respectively.

In Van Gelderen et al. [17], the model was modified to include two frequency offsets for myelin ( $\Delta f_{\text{my}-\text{ex}}$ ) and axonal ( $\Delta f_{\text{ax}-\text{ex}}$ ) water relative to extracellular water. This model was also fit to magnitude data:

$$|S_i(t)| = \left| A_{\text{my}}e^{-(1/T_{2,\text{my}}^* + i2\pi\Delta f_{\text{my}-\text{ex}})t} + A_{\text{ax}}e^{-(1/T_{2,\text{ax}}^* + i2\pi\Delta f_{\text{ax}-\text{ex}})t} + A_{\text{ex}}e^{-(1/T_{2,\text{ex}}^*)t} \right|. \quad (2)$$

In Nam et al. [11], the model was fit to the full complex data and further extended to include frequency offset terms for all three compartments with respect to the background as well as a background phase term  $\phi_0$ :

$$S_i(t) = \left[ A_{\text{my}}e^{-(1/T_{2,\text{my}}^* + i2\pi\Delta f_{\text{my}+\text{bg}})t} + A_{\text{ax}}e^{-(1/T_{2,\text{ax}}^* + i2\pi\Delta f_{\text{ax}+\text{bg}})t} + A_{\text{ex}}e^{-(1/T_{2,\text{ex}}^* + i2\pi\Delta f_{\text{ex}+\text{bg}})t} \right] e^{-i\phi_0}. \quad (3)$$

Our analysis focused on these final two models, which for simplicity we will refer to as the “magnitude fit” (Eqn. 2) and “complex fit” (Eqn. 3). Note that though Eqn. 2 is fit to magnitude data, it still represents a complex model with frequency shifts that produce asymmetric broadening of the water spectrum.

Model fitting was performed by first converting the preprocessed EPSI spectral data into the temporal domain using an inverse fast Fourier transform. The two models were then fit to the resulting voxel-wise

FIDs in Python using a non-linear least-squares approach implemented with the `curve_fit` function in the SciPy package. Optimization parameters for the fitting were identical to those presented in Table 1 of Nam et al. [11] and are available for reference in Supporting Information Table S1.

## 2.5 Asymmetry

To quantify asymmetric broadening of the water resonance, we use a unitless spectral asymmetry metric [14, 15, 32, 33]. At each voxel, the high-field half of the spectrum is subtracted from the low-field half and normalized by the total integral of the spectrum.

$$\text{Asymmetry}(x, y, z) = \frac{\int_0^{\nu_{\max}} f(x, y, z, \nu) d\nu - \int_{-\nu_{\max}}^0 f(x, y, z, \nu) d\nu}{\int_{-\nu_{\max}}^{\nu_{\max}} f(x, y, z, \nu) d\nu}, \quad (4)$$

where  $f(x, y, z, \nu)$  is the value of the water spectrum at a given position  $(x, y, z)$  and frequency  $\nu$ . Integration was performed to  $\nu_{\max} = \pm 38$  Hz from the main water peak (identified at 0 Hz for simplicity) to ensure that resonance details are captured while still reaching the spectral baseline. This cutoff value was shown in a previous study [15] to lead to asymmetry values sensitive to the presence of myelin. Overall, asymmetry results are robust to the specific choice of threshold (Supporting Information Figure S2). Integration was performed numerically in Python using the trapezoid rule. Before calculating asymmetry from the biophysical models, spectra were first computed by evaluating the analytic time-domain models at the echo points measured in the data using the parameters estimated for each voxel, then taking a fast Fourier transform.

## 2.6 dMRI processing

### 2.6.1 fODF fitting and registration

The dMRI datasets and associated b-vectors were first manually rotated so that the axes aligned with the EPSI data. Subsequent processing was performed with the MRtrix3 software package [34]. Data were denoised using the `dwidenoise` routine [35, 36]. Binary brain masks were generated with the `dwi2mask` routine to speed further processing. The datasets were fit to a tensor model [37] using `dwi2tensor` to calculate the fractional anisotropy (FA) metric used as a proxy for white matter content. The data were then fit to fiber orientation distribution functions (fODFs) using constrained spherical deconvolution [38, 39] to estimate the orientation of the principal fiber populations and to evaluate the presence of additional crossing fiber populations within each voxel. Comparison of fODFs across datasets requires global intensity normalization of the diffusion data prior to reconstruction, since the data are not first log-normalized with the  $b_0$  volume. First, the data were bias-corrected using the `N4BiasFieldCorrection` algorithm [40] in ANTs, then global intensity normalization was done with the `dwinormalise group` routine in MRTrax3. White matter response functions were then calculated for each dataset using the `tournier` algorithm [41], with  $\ell_{\max} = 6$

(28 coefficients). The group-averaged response function was then used to fit the bias-corrected diffusion-weighted images to fODFs with the `dwi2fod` command.

The FA images were spatially registered to the corresponding EPSI peak-height images using affine transformations calculated in ANTs using a mutual information maximization approach. The FA images were chosen for registration because they exhibit greater white/gray matter contrast, particularly for the shiverer data. The resulting affine transformations were used to warp, reorient [42], and modulate [43] the fODFs using the `mrtransform` command in MRTrix3, which preserves apparent fiber densities across fODF lobes before and after spatial transformation.

## 2.6.2 Microstructural analysis

As in Foxley et al. [15], voxels across the entire dataset were binned according to FA value with thresholds of  $FA \leq 0.3$ ,  $0.3 < FA \leq 0.45$ ,  $0.45 < FA \leq 0.6$ , and  $FA > 0.6$ . Visual inspection of the resulting voxel masks suggests that the lower  $FA \leq 0.3$  bin consists of predominately gray matter while the upper  $FA > 0.6$  bin consists of predominately white matter, with the additional two bins composed of mixed populations. To account for known biases in FA in voxels with crossing fibers [44], voxels were further characterized by the number of distinct fiber populations. Individual lobes of each fODF were segmented in MRTrix3 using the `fod2fixel` and `fixel2peaks` commands. The number of populations ( $N_f$ ) at each voxel was recorded as either “single” ( $N_f = 1$ ) or “crossing” ( $N_f > 1$ ). Voxel-wise changes in  $T_2^*$  [45, 46] and spectral asymmetry [14, 15] have been observed to change as a function of the angle between the orientation of the principal fiber populations and  $B_0$ , which has been described as evidence of the susceptibility anisotropy of myelin [20, 46–48]. To explore this effect in the model-derived spectra, the angle between principal fiber orientations and  $B_0$  was calculated as  $\Gamma = \cos^{-1}(s_z)$ , where  $\hat{s} = (s_x, s_y, s_z)$  is the fiber orientation unit vector at a given voxel and  $B_0$  points along  $\hat{s}_{B_0} = (0, 0, 1)$ . Due to the symmetry of the fODFs,  $\Gamma$  values were manually constrained to be within  $[0^\circ, 90^\circ]$ . Voxels across the entire dataset were pooled by angle into bins in  $5^\circ$  increments. The voxel counts across all values of FA,  $N_f$ , and  $\Gamma$  are shown for both control and shiverer data in Figure 1.

## 3 Results

### 3.1 Comparison of asymmetry values

Figure 2 shows the distribution of asymmetry values calculated from the raw data and both models across all voxels from control and shiverer samples. At the whole-brain level there is a small but clear separation between control and shiverer asymmetry values observed in the data, whereas both model-derived asymmetry distributions are virtually indistinguishable between control and shiverer. Spectra derived from each of the two biophysical models also dramatically underestimate the range of asymmetry magnitudes observed in

the data. Across all voxels in both tissue types, data-derived asymmetry has a standard deviation of 0.0427, while the magnitude- and complex-fit asymmetries have standard deviations of 0.0140 and 0.0058,

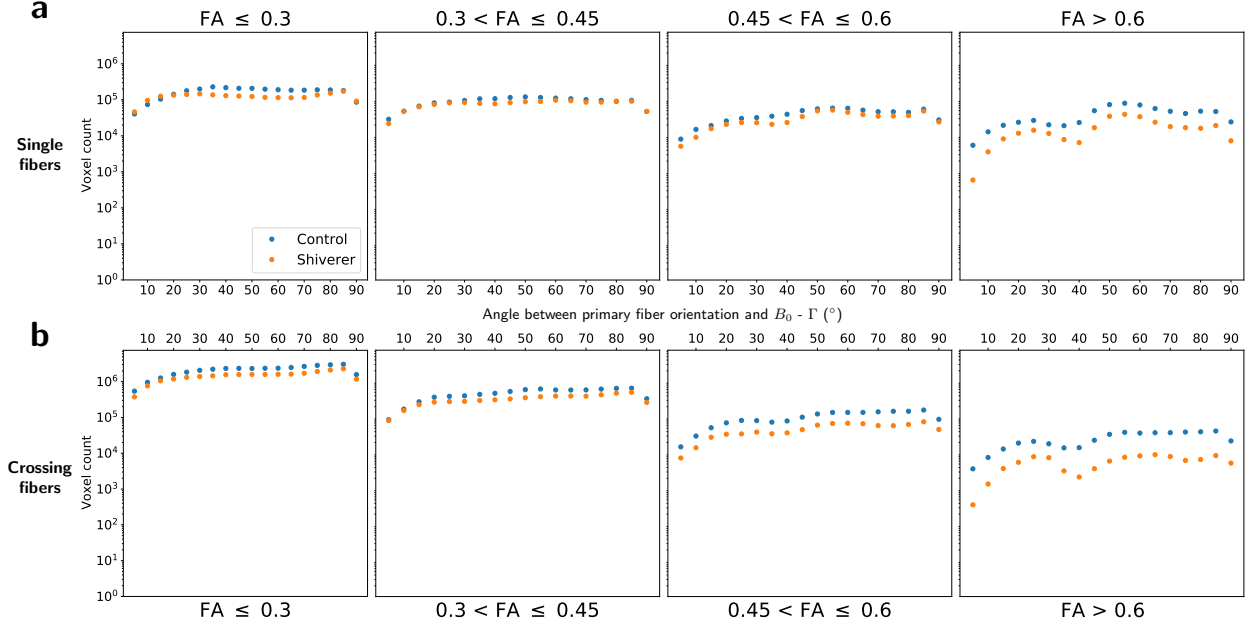


Figure 1: Voxel counts for control (blue) and shiverer (orange) data across FA and angular bins for voxels with (a) single and (b) crossing fiber populations.

respectively.

Voxel-wise comparisons between data- and model-derived asymmetries are shown as scatterplots across different FA bins in Figure 3. Asymmetries from the magnitude-fit model show negligible correlation ( $R^2 \approx 0$ ) with data-derived asymmetries from both control and shiverer samples across all FA bins. The complex-fit model performs slightly better, with  $R^2$  values that increase with increasing FA for control data, up to a maximum of  $R^2 = 0.403$  for the highest FA bin. Complex-fit correlations are lower in shiverer data than in control data and do not increase with FA.

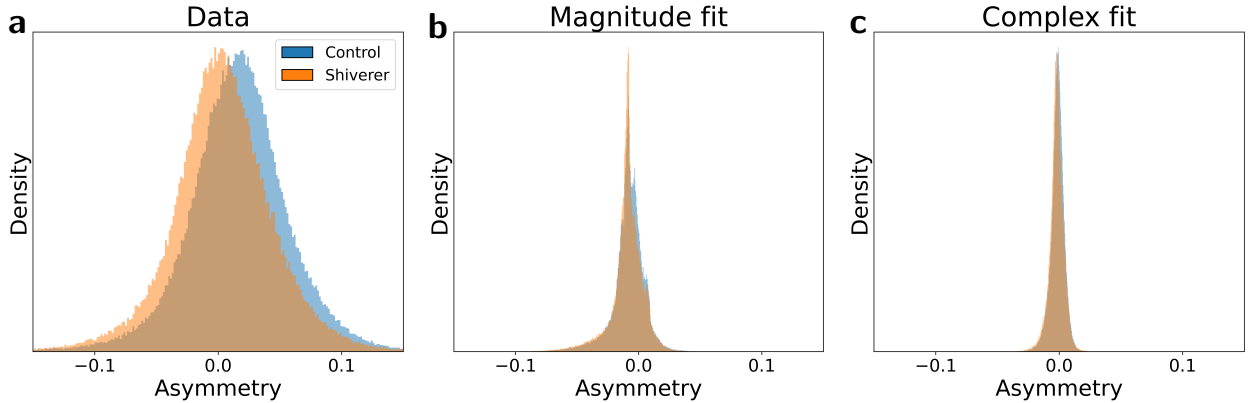


Figure 2: Histograms of asymmetries from spectra derived from (a) data, (b) the magnitude-fit model, and (c) the complex-fit model.

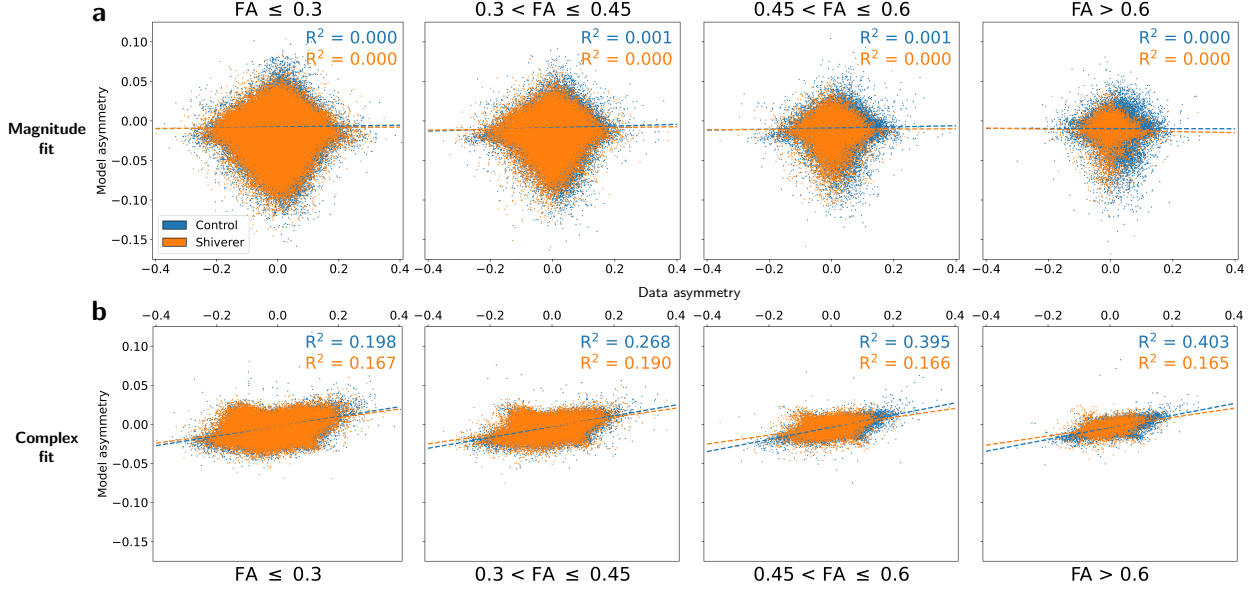


Figure 3: Scatterplots of data- and model-derived asymmetries for the (a) magnitude-fit and (b) complex-fit models. Dashed lines represent the results of linear regressions and the  $R^2$  values are the square of the Pearson correlation coefficients.

Figure 4 shows 2D histograms of (1) the absolute asymmetry difference between the models and data vs. (2) the adjusted  $R^2$  assessing the goodness-of-fit of the models to the FID data for voxels with  $FA > 0.6$ . Both models generally fit the FID data very well overall, with the mean adjusted  $R^2$  values across all voxels from both tissue types being 0.994 and 0.988 for the magnitude-fit and complex-fit models, respectively. However, the high adjusted  $R^2$  of the models in the temporal domain does not correspond to accuracy in reproducing the asymmetric spectral broadening observed in the data — correlations between the adjusted  $R^2$  and asymmetry difference are negligible for both models. This effect is visually demonstrated further in Figure 4c, which shows two representative white-matter voxels from the anterior commissure tract of a control mouse. In both sample voxels, the two models fit very closely to the data in the temporal domain (adjusted  $R^2 > 0.98$ ) but greatly underestimate asymmetry in the frequency domain. For example, in the case of the voxel highlighted in green, both models clearly miss a prominent secondary peak around 8 Hz (black arrow in Figure 4c, bottom right) corresponding to an oscillation in the FID around 0.05-0.18 seconds.

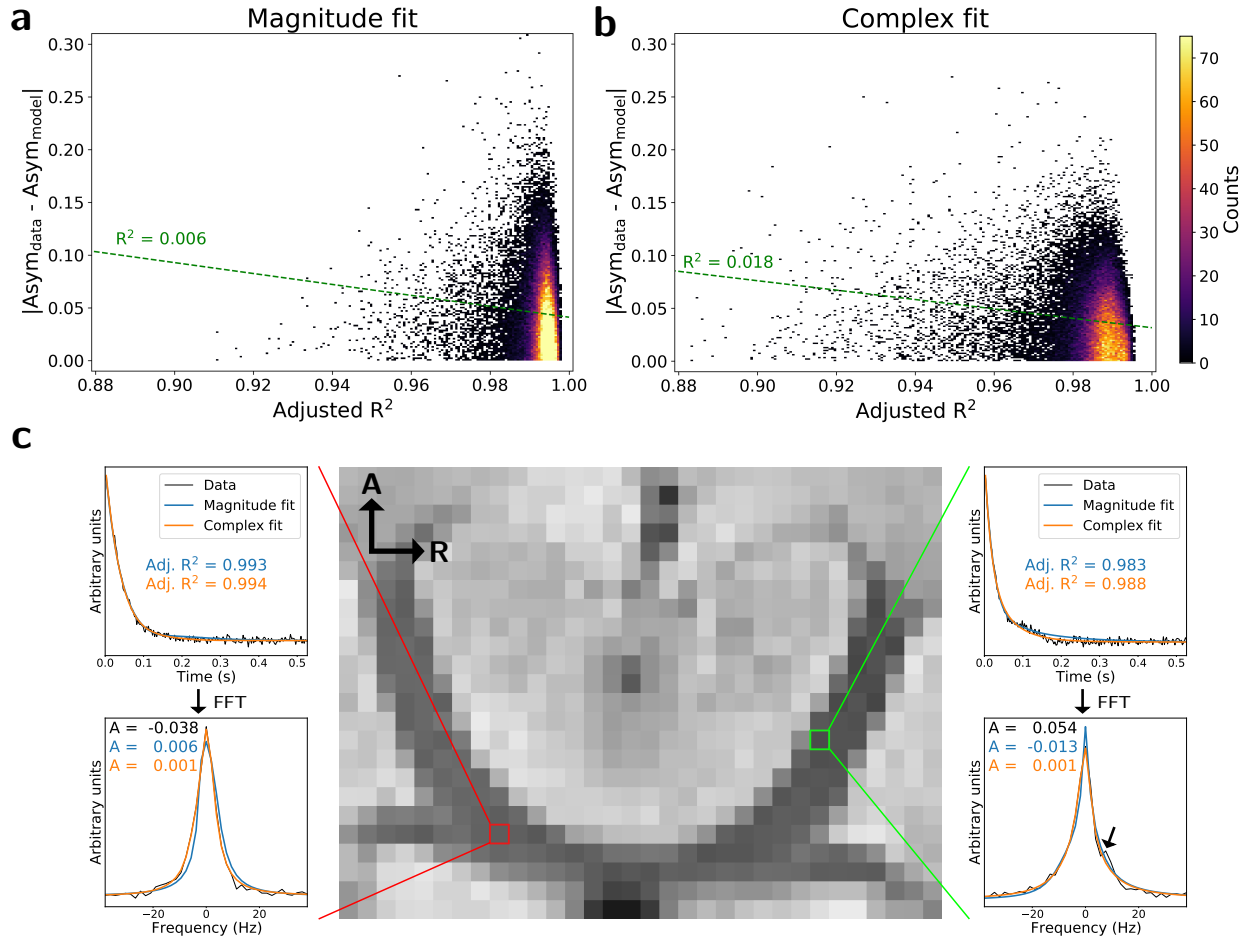


Figure 4: (a-b) 2D histograms of the absolute difference between measured and model-estimated asymmetries vs. the model goodness-of-fit in terms of adjusted  $R^2$  for the (a) magnitude-fit and (b) complex-fit models for voxels with FA > 0.6. Green dashed lines show linear regressions with associated  $R^2$  values indicating a negligible relationship. (c) Water peak-height image showing the anterior commissure tract of a control mouse with two representative voxels demonstrating the mismatch between the model goodness-of-fit and asymmetry difference. A–R axis labels correspond to the Anterior and Right directions, respectively.

Figure 5 shows additional 2D histograms for high FA (FA > 0.6) voxels demonstrating the relationship between the asymmetry directly measured in the spectral data and the compartmental frequency shifts predicted by the models. Note that the magnitude-fit model (Eqn. 2) includes frequency shift terms for two compartments:  $\Delta f_{my-ex}$  and  $\Delta f_{ax-ex}$ , defined as the difference between the myelin and axonal water shift with the extracellular water shift, respectively. The complex-fit model (Eqn. 3) includes frequency shift terms for all three components:  $\Delta f_{my+bg}$ ,  $\Delta f_{ax+bg}$ ,  $\Delta f_{ex+bg}$ , defined as the additional shifts in myelin, axonal, and extracellular water, respectively, above a background. For consistent comparison between the two models, the extracellular shifts have been subtracted from the complex-fit model frequencies reported in Figure 5. The magnitude-fit frequencies again show virtually no correlation with the measured asymmetry, while the complex-model frequencies show only weak correlation ( $R^2 = 0.114$ ) in the axonal compartment.

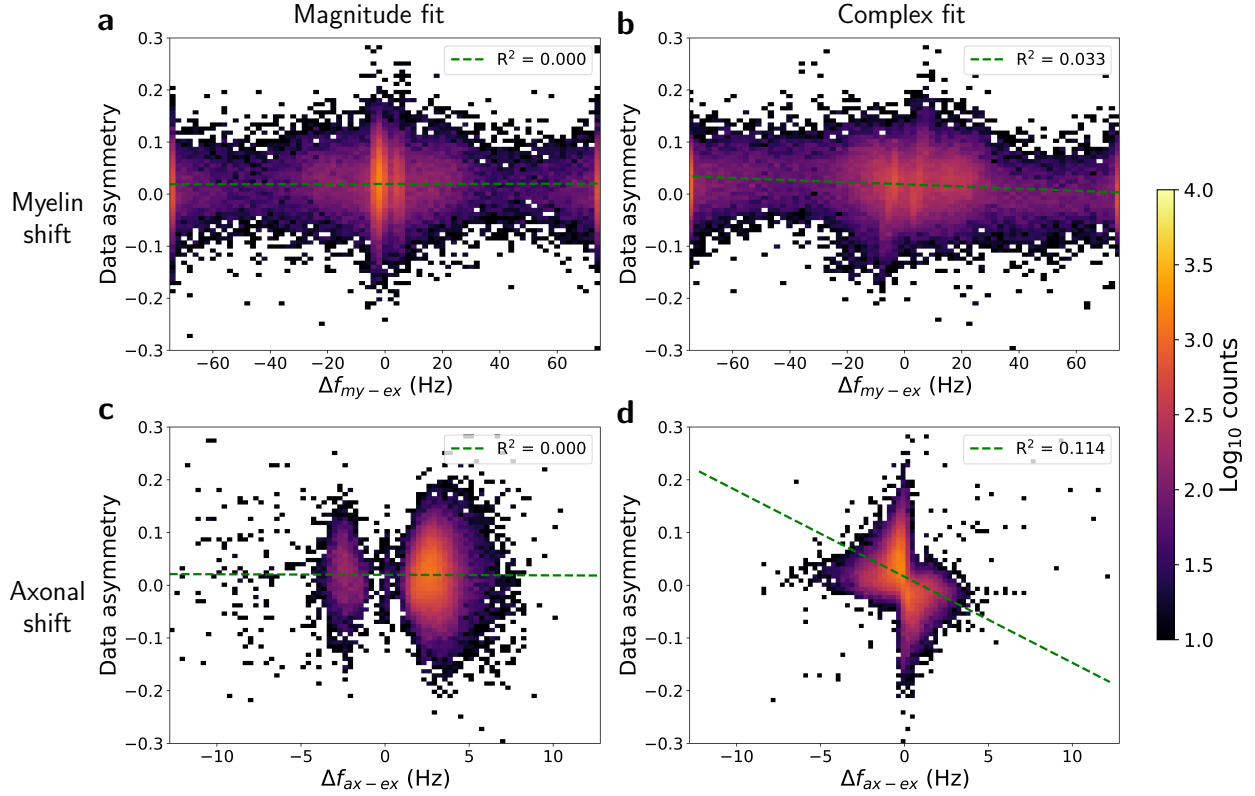


Figure 5: 2D histograms showing the relationship between data asymmetry and model-predicted frequency shifts for the myelin and axonal water compartments in voxels with FA > 0.6. Green dashed lines show linear regressions with associated  $R^2$  values.

### 3.2 Sensitivity to myelin

While Figure 2 showed the range of asymmetry values across the entire dataset, Figure 6 shows data- and model-derived asymmetry distributions broken down by FA bin for single- and crossing-fiber voxels. Previous work has shown that data-derived spectral asymmetry is sensitive to myelin [15], with spectra exhibiting consistent upfield broadening along white-matter tracts in control mice that decreases in magnitude in shiverer mice. This is demonstrated in Figures 6a–b, which show an increasing separation between control and shiverer data-derived asymmetries as FA increases, independent of the number of fiber populations. This effect is not observed to the same extent after fitting the data to models, as shown in Figures 6c–f. The separation between the control and shiverer distributions is quantified in Figure 7 by treating spectral asymmetry as a one-variable classifier and reporting the resulting area under the receiver operating characteristic curve (AUC) as a function of FA for single- and crossing-fiber voxels. A value of 0.5 is consistent with a “random guessing” classifier (i.e. no separation), while a value of 1.0 indicates perfect classification (i.e. complete separation). While separation between the control and shiverer distributions did increase marginally with FA for both models, data-derived asymmetry led to a substantially higher AUC

than either of the model-based approaches under all microstructural conditions. Notably, the performance of data-derived asymmetry in classifying control from shiverer tissue was robust to the number of fiber populations, with only slight decreases in AUC for higher FA voxels with crossing fibers ( $FA > 0.45$ ) compared to single fibers and slight increases for lower FA voxels with crossing fibers ( $FA \leq 0.45$ ) compared to single fibers, potentially owing to the fact that voxels with tightly packed, coherent fibers are likely to lead to artificially low FA values if they contain multiple distinct populations.

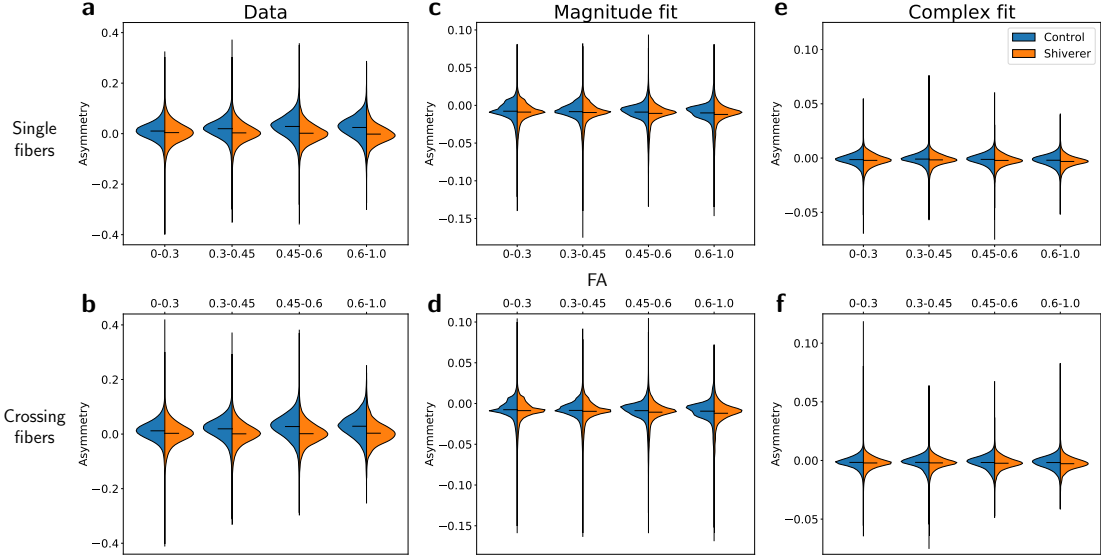


Figure 6: Violin plots illustrating distributions of control and shiverer asymmetries derived from (a–b) data, (c–d) the magnitude-fit model, and (e–f) the complex-fit model as a function of FA bin for voxels with single (a,c,e) and crossing (b,d,f) fibers. Distribution means are indicated by black lines. Note the difference in y-axis limits between (a–b), (c–d), and (e–f).

The myelin sensitivity of the data-derived asymmetry is further demonstrated in the left column of Figure 8, which shows representative coronal slices of asymmetry images. While the data-derived asymmetry leads to observable gray/white-matter contrast in the control image, asymmetry images calculated from each of the models show markedly lower contrast, with virtually no distinguishable white matter tracts visible in the images derived from the magnitude-fit model in particular.

To explore the sensitivity of the models to the susceptibility anisotropy of myelin, Figure 9 shows the mean asymmetry as a function of  $\Gamma$ , the angle between the orientation of the primary fiber population and  $B_0$  for voxels with  $FA \geq 0.6$ . Color-shaded regions represent the interquartile range (25–75th percentile) across all voxels within each angular bin, and gray-shaded regions represent regions where the difference between control and shiverer values was not found to be statistically significant using a t-test with  $\alpha = 0.01$  after correcting for multiple comparisons. Both the data and the complex-fit asymmetry values show a clear relationship between asymmetry and  $\Gamma$  with good agreement with the susceptibility anisotropy model [46],

$$\text{asym}(\Gamma) = c_0 + c_1 \sin(2\Gamma + \phi_0) + c_2 \sin(4\Gamma + \phi_1), \quad (5)$$

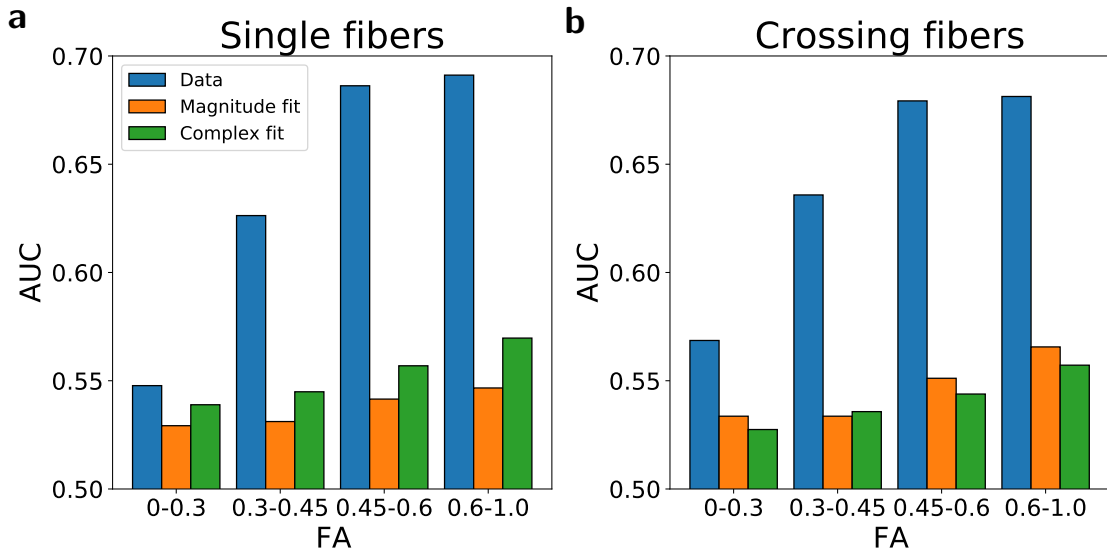


Figure 7: Values for the area under the ROC curve (AUC) using asymmetry as a one-variable classifier for control vs. shiverer data. Values represent AUCs for subsets of voxels in different FA bins containing either (a) single or (b) crossing fiber populations.

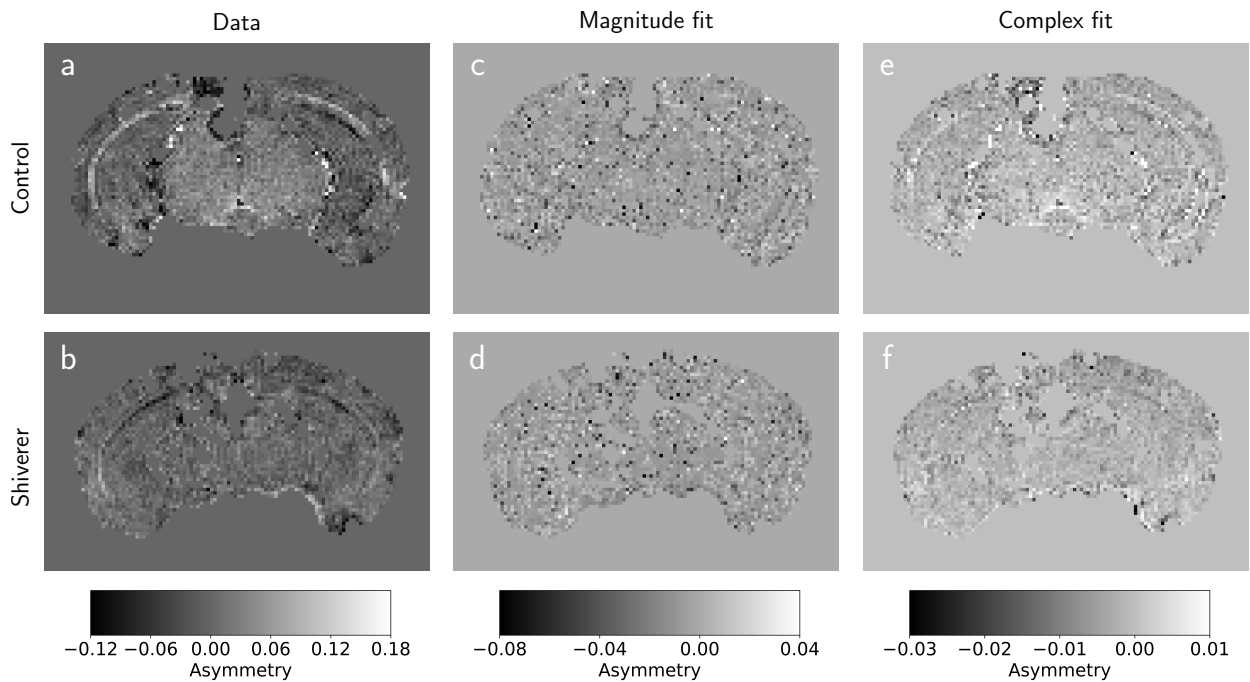


Figure 8: Representative coronal slices of spectral asymmetry images derived from (top) control and (bottom) shiverer samples, with asymmetry calculated from (left) data, (center) the magnitude-fit model, and (right) the complex-fit model.

though the angular effect is much less pronounced for the magnitude-fit model and both models once again show far less separation between control and shiverer values than observed from the data before model-

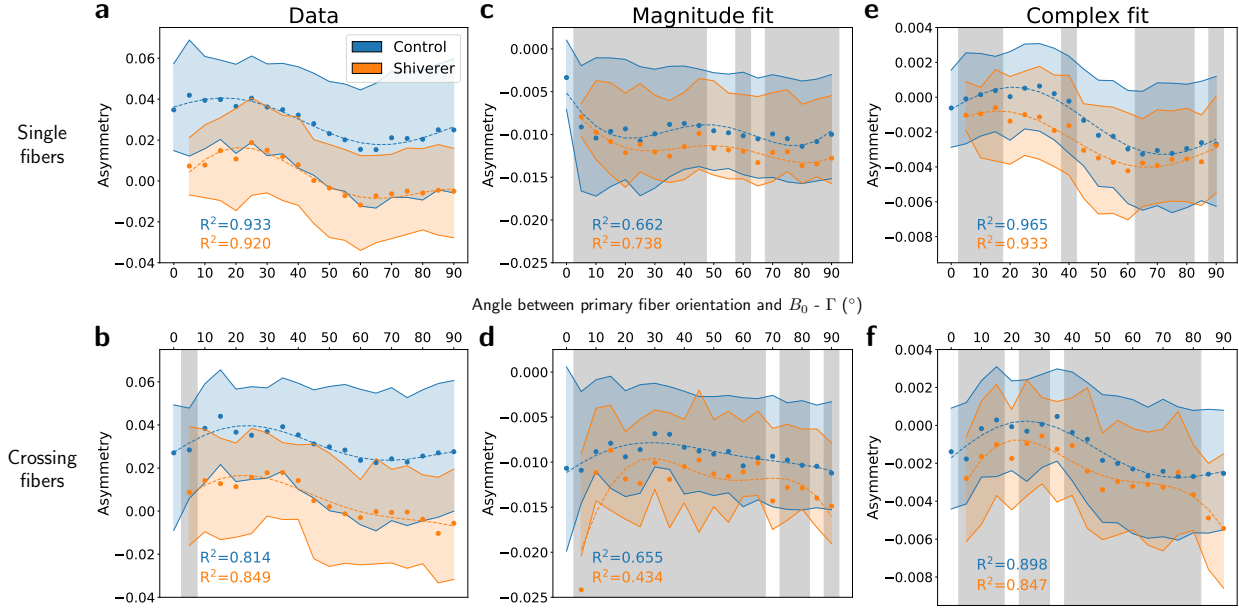


Figure 9: Relationship between asymmetry and  $\Gamma$ , the angle between the orientation of the primary fiber population and  $B_0$  for (a–b) data (c–d) the magnitude-fit model, and (e–f) the complex-fit model. Points represent averages within angular bins with a width of  $5^\circ$  across all voxels with  $FA \geq 0.6$  containing either (a,c,e) single fibers or (b,d,f) crossing fibers. Color-shaded regions represent the interquartile range (25–75th percentiles) across all voxels. Dotted lines represent fits to the susceptibility anisotropy model with associated adjusted  $R^2$  values. Gray regions represent angular bins for which the difference between control and shiverer values was not found to be significant with a t-test at  $\alpha = 0.01$ .

fitting.

## 4 Discussion

This study aimed to characterize the extent to which water spectra derived from two biophysical signal models fit to EPSI MRI data are able to replicate the spectral characteristics observed directly from the data itself, specifically with respect to sensitivity to myelin. We used spectral asymmetry around the main water peak as a summary metric to explore how data- and model-derived spectra differ over a range of microstructural environments, covering variations in white matter content using FA as a proxy metric, the role of crossing fibers, and the angle between the orientation of the primary fiber population and  $B_0$ . Our overall finding is that independent of how well the models fit the temporal FID data, neither model was able to accurately reproduce the asymmetric broadening observed directly in the data. The simplicity of the models provides interpretability and computational advantage at the expense of failing to capture the full complexity of the spectra. This results in a dramatic underestimation of the magnitude of the asymmetric broadening effect (Figure 2), with model-derived values for asymmetry that only loosely correlate with those measured in the data in high-FA voxels (Figure 3). Most importantly, the process of fitting the data to these simple biophysical models effectively leads to compromised spectral sensitivity to myelin under all microstructural

conditions explored in this work (Figure 7–8).

While the above conclusions apply broadly to both the magnitude- and complex-fit models, the complex-fit model did perform better with respect to certain spectral characteristics, a finding consistent with previous work comparing these two models [11]. Complex-fit asymmetries correlated more strongly with data-measured asymmetries in both control and shiverer tissues across all FA bins (Figure 3) than did magnitude-fit asymmetries. Similarly, the axonal water compartment frequency shift estimated from the complex-fit model was the only compartmental frequency shown to have any correlation with the raw-data asymmetry (Figure 5). Complex-fit asymmetries were also shown to have a stronger relationship between the fiber orientation and  $B_0$  than magnitude-fit asymmetries (Figure 9), though the complex-fit model showed only modest improvements over the magnitude-fit model on overall myelin sensitivity and white matter contrast (Figures 7–8).

The data-derived asymmetry results presented in this work are consistent with previous studies demonstrating the utility of model-free analysis of fully-sampled MGE/EPSI data in the frequency domain towards myelin imaging [13–15]. This work extends such analyses to quantify biases in existing biophysical models due in part to the simplicity of their underlying geometric assumptions [20]. Through full sampling of the FID to the noise floor, our results indicate that these biases are indeed present in the explored compartmental models even at the level of compressing the full spectral information into a single scalar asymmetry metric, promoting caution in the downstream interpretation of model-predicted spectra.

Notably, this work also demonstrates the robustness of the asymmetry metric under complex microstructural conditions. Measured asymmetries were shown to have comparable sensitivities to myelin (Figure 7) and demonstrate similar behavior with respect to fiber angle (Figure 9) in voxels with single and crossing fibers. A direction of future work will be to more rigorously characterize the spectral response to the specific number as well as relative strength and position of fiber populations within the voxel.

This analysis method of benchmarking spectroscopic MR data in the temporal domain against data in the spectral domain can be extended to existing datasets after applying a linear transform to the FID to produce absorption spectra. We note, however, the importance of sampling to the results in this work – spectral sensitivity to myelin is dependent on the increased spectral resolution that comes by sampling the FID into the noise floor. Supporting Information Figure S3 shows AUCs similar to Figure 7, and demonstrates that after truncating the FID to just the first 32 echoes, neither the data- nor the model-derived asymmetries show meaningful sensitivity to myelin, while Supporting Information Figure S4 shows that myelin sensitivity as represented by the AUC stabilizes for data-derived asymmetry around 64 echoes.

As in previous work [15], the response of asymmetry to fiber angle was shown to be present, but diminished in magnitude in dysmyelinated shiverer mice relative to control mice. Incorporating full demyelination models in future studies will help further clarify the role of myelin in driving asymmetric broadening of the spectrum. More robust analysis of data from control and fully demyelinated mice will also help to identify specific spectral features beyond asymmetry that could potentially form new imaging biomarkers

and motivate the development of new biophysical models that remain interpretable and clinically useful without compromising myelin sensitivity. Such analysis together with the use of novel multi-scale, multi-modal preclinical imaging pipelines [49] could help further elucidate the role of susceptibility anisotropy and other microstructural drivers of the MR signal.

## 5 Conclusion

Through analysis of fully-sampled spectra from control and dysmyelinated mouse brain, we quantify biases in existing biophysical compartmental models traditionally used for myelin imaging with spectroscopic data. We showed that spectra estimated from these biophysical models fail to accurately predict the extent of asymmetric broadening attributable in part to myelin, leading ultimately to compromised myelin sensitivity in the estimated spectra. This work further demonstrates the utility of model-free analysis of the water resonance spectrum with fully-sampled EPSI data, promoting its continued development as a tool to benchmark novel biophysical signal models and as a potential future *in vivo* MRI biomarker for dysmyelination.

## 6 Acknowledgments

S.T. is supported by the National Institutes of Health (NIH) (F31NS113571). N.K. is supported by the NIH Brain Initiative (U01MH109100). P.L.R. is partially supported by the NIH (R01EB026300). Additional funding was provided by the NIH (S10OD025081, S10RR021039, P30CA14599).

## References

1. C. Stadelmann, S. Timmler, A. Barrantes-Freer, *et al.*, "Myelin in the central nervous system: Structure, function, and pathology", *Physiological Reviews*, vol. 99, no. 3, pp. 1381–1431, Jul. 2019, ISSN: 15221210. DOI: [10.1152/physrev.00031.2018](https://doi.org/10.1152/physrev.00031.2018).
2. M. S. van der Knaap and M. Bugiani, *Leukodystrophies: a proposed classification system based on pathological changes and pathogenetic mechanisms*, Sep. 2017. DOI: [10.1007/s00401-017-1739-1](https://doi.org/10.1007/s00401-017-1739-1).
3. M. Arshad, J. A. Stanley, and N. Raz, "Test-retest reliability and concurrent validity of *in vivo* myelin content indices: Myelin water fraction and calibrated T1w/T2w image ratio", *Human Brain Mapping*, vol. 38, no. 4, pp. 1780–1790, Apr. 2017, ISSN: 10970193. DOI: [10.1002/hbm.23481](https://doi.org/10.1002/hbm.23481).
4. S. Haller, E. Kövari, F. R. Herrmann, *et al.*, "Do brain T2/FLAIR white matter hyperintensities correspond to myelin loss in normal aging? A radiologic-neuropathologic correlation study", *Acta Neuropathologica Communications*, vol. 2, no. 1, p. 14, Jan. 2014, ISSN: 20515960. DOI: [10.1186/2051-5960-1-14](https://doi.org/10.1186/2051-5960-1-14). [Online]. Available: <https://actaneurocomms.biomedcentral.com/articles/10.1186/2051-5960-1-14>.
5. M. N. Uddin, T. D. Figley, R. A. Marrie, *et al.*, "Can T1w/ T2w ratio be used as a myelin-specific measure in subcortical structures? Comparisons between FSE-based T2w/ T2w ratios, GRASE-based T1w/ T2w ratios and multi-echo GRASE-based myelin water fractions", *NMR in Biomedicine*, vol. 31, no. 3, e3868, Mar. 2018, ISSN: 09523480. DOI: [10.1002/nbm.3868](https://doi.org/10.1002/nbm.3868). [Online]. Available: <http://doi.wiley.com/10.1002/nbm.3868>.
6. A. Mackay, K. Whittall, J. Adler, *et al.*, "In vivo visualization of myelin water in brain by magnetic resonance", *Magnetic Resonance in Medicine*, vol. 31, no. 6, pp. 673–677, Jun. 1994, ISSN: 15222594. DOI: [10.1002/mrm.1910310614](https://doi.org/10.1002/mrm.1910310614).

7. A. L. MacKay and C. Laule, "Magnetic Resonance of Myelin Water: An in vivo Marker for Myelin", *Brain Plasticity*, vol. 2, no. 1, pp. 71–91, Nov. 2016, ISSN: 22136304. DOI: [10.3233/bpl-160033](https://doi.org/10.3233/bpl-160033).
8. Y. P. Du, R. Chu, D. Hwang, *et al.*, "Fast multislice mapping of the myelin water fraction using multicompartment analysis of T2\* decay at 3T: A preliminary postmortem study", *Magnetic Resonance in Medicine*, vol. 58, no. 5, pp. 865–870, Nov. 2007, ISSN: 07403194. DOI: [10.1002/mrm.21409](https://doi.org/10.1002/mrm.21409).
9. O. I. Kwon, E. J. Woo, Y. P. Du, *et al.*, "A tissue-relaxation-dependent neighboring method for robust mapping of the myelin water fraction", *NeuroImage*, vol. 74, pp. 12–21, Jul. 2013, ISSN: 10538119. DOI: [10.1016/j.neuroimage.2013.01.064](https://doi.org/10.1016/j.neuroimage.2013.01.064).
10. C. Lenz, M. Klarhöfer, and K. Scheffler, "Feasibility of in vivo myelin water imaging using 3D multigradient-echo pulse sequences", *Magnetic Resonance in Medicine*, vol. 68, no. 2, pp. 523–528, Aug. 2012, ISSN: 07403194. DOI: [10.1002/mrm.23241](https://doi.org/10.1002/mrm.23241). [Online]. Available: <http://doi.wiley.com/10.1002/mrm.23241>.
11. Y. Nam, J. Lee, D. Hwang, *et al.*, "Improved estimation of myelin water fraction using complex model fitting", *NeuroImage*, vol. 116, pp. 214–221, Aug. 2015, ISSN: 10538119. DOI: [10.1016/j.neuroimage.2015.03.081](https://doi.org/10.1016/j.neuroimage.2015.03.081). [Online]. Available: <https://linkinghub.elsevier.com/retrieve/pii/S1053811915002773>.
12. P. Sati, P. van Gelderen, A. C. Silva, *et al.*, "Microcompartment specific T2\* relaxation in the brain", *NeuroImage*, vol. 77, pp. 268–278, Aug. 2013, ISSN: 10538119. DOI: [10.1016/j.neuroimage.2013.03.005](https://doi.org/10.1016/j.neuroimage.2013.03.005).
13. S. Foxley, M. Domowicz, G. S. Karczmar, *et al.*, "3D high spectral and spatial resolution imaging of ex vivo mouse brain", *Medical Physics*, vol. 42, no. 3, pp. 1463–1472, Mar. 2015, ISSN: 00942405. DOI: [10.1118/1.4908203](https://doi.org/10.1118/1.4908203).
14. S. Foxley, G. S. Karczmar, and K. Takahashi, "The effects of variations in tissue microstructure from postmortem rat brain on the asymmetry of the water proton resonance", *Magnetic Resonance in Medicine*, Jul. 2018, ISSN: 07403194. DOI: [10.1002/mrm.27338](https://doi.org/10.1002/mrm.27338). [Online]. Available: <http://doi.wiley.com/10.1002/mrm.27338>.
15. S. Foxley, G. Wildenberg, V. Sampathkumar, *et al.*, "Sensitivity to myelin using model-free analysis of the water resonance line-shape in postmortem mouse brain", *Magnetic Resonance in Medicine*, mrm.28440, Jul. 2020, ISSN: 0740-3194. DOI: [10.1002/mrm.28440](https://doi.org/10.1002/mrm.28440). [Online]. Available: <https://onlinelibrary.wiley.com/doi/abs/10.1002/mrm.28440>.
16. D. Hwang, D. H. Kim, and Y. P. Du, "In vivo multi-slice mapping of myelin water content using T2\* decay", *NeuroImage*, vol. 52, no. 1, pp. 198–204, Aug. 2010, ISSN: 10538119. DOI: [10.1016/j.neuroimage.2010.04.023](https://doi.org/10.1016/j.neuroimage.2010.04.023).
17. P. van Gelderen, J. A. de Zwart, J. Lee, *et al.*, "Nonexponential T 2 \* decay in white matter", *Magnetic Resonance in Medicine*, vol. 67, no. 1, pp. 110–117, Jan. 2012, ISSN: 07403194. DOI: [10.1002/mrm.22990](https://doi.org/10.1002/mrm.22990). [Online]. Available: <http://doi.wiley.com/10.1002/mrm.22990>.
18. S. Wharton and R. Bowtell, "Fiber orientation-dependent white matter contrast in gradient echo MRI", *Proceedings of the National Academy of Sciences of the United States of America*, vol. 109, no. 45, pp. 18559–18564, Nov. 2012, ISSN: 00278424. DOI: [10.1073/pnas.1211075109](https://doi.org/10.1073/pnas.1211075109).
19. W. C. Chen, S. Foxley, and K. L. Miller, "Detecting microstructural properties of white matter based on compartmentalization of magnetic susceptibility", *NeuroImage*, vol. 70, pp. 1–9, Apr. 2013, ISSN: 10538119. DOI: [10.1016/j.neuroimage.2012.12.032](https://doi.org/10.1016/j.neuroimage.2012.12.032).
20. T. Xu, S. Foxley, M. Kleinnijenhuis, *et al.*, "The effect of realistic geometries on the susceptibility-weighted MR signal in white matter", *Magnetic Resonance in Medicine*, vol. 79, no. 1, pp. 489–500, Jan. 2018, ISSN: 07403194. DOI: [10.1002/mrm.26689](https://doi.org/10.1002/mrm.26689). [Online]. Available: <http://doi.wiley.com/10.1002/mrm.26689>.
21. J. Rosenbluth, "Central myelin in the mouse mutant shiverer", *Journal of Comparative Neurology*, vol. 194, no. 3, pp. 639–648, Dec. 1980, ISSN: 10969861. DOI: [10.1002/cne.901940310](https://doi.org/10.1002/cne.901940310).
22. W. Du, G. S. Karczmar, S. J. Uftring, *et al.*, "Anatomical and functional brain imaging using high-resolution echo-planar spectroscopic imaging at 1.5 Tesla", *NMR in Biomedicine*, vol. 18, no. 4, pp. 235–241, Jun. 2005, ISSN: 0952-3480. DOI: [10.1002/nbm.952](https://doi.org/10.1002/nbm.952). [Online]. Available: <http://doi.wiley.com/10.1002/nbm.952>.
23. S. Foxley, X. Guo, and G. S. Karczmar, "Functional brain imaging with high spectral and spatial resolution MRI at 3T", in *25th Annual Meeting and Exhibition of the International Society of Magnetic Resonance in Medicine*, Honolulu, HI, USA, 2017, p. 5261.
24. W. Du, Y. P. Du, X. Fan, *et al.*, "Reduction of spectral ghost artifacts in high-resolution echo-planar spectroscopic imaging of water and fat resonances", *Magnetic Resonance in Medicine*, vol. 49, no. 6, pp. 1113–1120, Jun. 2003, ISSN: 0740-3194. DOI: [10.1002/mrm.10485](https://doi.org/10.1002/mrm.10485). [Online]. Available: <http://doi.wiley.com/10.1002/mrm.10485>.
25. X. Fan, W. Du, P. MacEneaney, *et al.*, "Structure of the water resonance in small voxels in rat brain detected with high spectral and spatial resolution MRI", *Journal of Magnetic Resonance Imaging*, vol. 16, no. 5, pp. 547–552, Nov. 2002, ISSN: 1053-1807. DOI: [10.1002/jmri.10193](https://doi.org/10.1002/jmri.10193). [Online]. Available: <http://doi.wiley.com/10.1002/jmri.10193>.
26. H. de Brouwer, "Evaluation of algorithms for automated phase correction of NMR spectra", *Journal of Magnetic Resonance*, vol. 201, no. 2,

- pp. 230–238, Dec. 2009, ISSN: 10907807. DOI: [10.1002/jmr.2009.09.017](https://doi.org/10.1002/jmr.2009.09.017).
27. H. A. Al-Hallaq, X. Fan, M. Zamora, *et al.*, “Spectrally inhomogeneous BOLD contrast changes detected in rodent tumors with high spectral and spatial resolution MRI”, *NMR in Biomedicine*, vol. 15, no. 1, pp. 28–36, Feb. 2002, ISSN: 0952-3480. DOI: [10.1002/nbm.728](https://doi.org/10.1002/nbm.728). [Online]. Available: <http://doi.wiley.com/10.1002/nbm.728>.
28. T. Liu, I. Khalidov, L. de Rochefort, *et al.*, “A novel background field removal method for MRI using projection onto dipole fields (PDF)”, *NMR in Biomedicine*, vol. 24, no. 9, pp. 1129–1136, Nov. 2011, ISSN: 09523480. DOI: [10.1002/nbm.1670](https://doi.org/10.1002/nbm.1670). [Online]. Available: <http://doi.wiley.com/10.1002/nbm.1670>.
29. F. Schweser, A. Deistung, B. W. Lehr, *et al.*, “Quantitative imaging of intrinsic magnetic tissue properties using MRI signal phase: An approach to *in vivo* brain iron metabolism?”, *NeuroImage*, vol. 54, no. 4, pp. 2789–2807, Feb. 2011, ISSN: 10538119. DOI: [10.1016/j.neuroimage.2010.10.070](https://doi.org/10.1016/j.neuroimage.2010.10.070).
30. B. B. Avants, N. J. Tustison, J. Wu, *et al.*, “An Open Source Multivariate Framework for n-Tissue Segmentation with Evaluation on Public Data”, *Neuroinformatics*, vol. 9, no. 4, pp. 381–400, Dec. 2011, ISSN: 1539-2791. DOI: [10.1007/s12021-011-9109-y](https://doi.org/10.1007/s12021-011-9109-y). [Online]. Available: <http://link.springer.com/10.1007/s12021-011-9109-y>.
31. S. M. Smith, “Fast robust automated brain extraction”, *Human Brain Mapping*, vol. 17, no. 3, pp. 143–155, Nov. 2002, ISSN: 10659471. DOI: [10.1002/hbm.10062](https://doi.org/10.1002/hbm.10062).
32. S. Foxley, X. Fan, D. Mustafi, *et al.*, “Sensitivity to tumor microvasculature without contrast agents in high spectral and spatial resolution MR images”, *Magnetic Resonance in Medicine*, vol. 61, no. 2, pp. 291–298, Feb. 2009, ISSN: 07403194. DOI: [10.1002/mrm.21801](https://doi.org/10.1002/mrm.21801). [Online]. Available: <http://doi.wiley.com/10.1002/mrm.21801>.
33. K. L. Miller, “Asymmetries of the balanced SSFP profile. Part I: Theory and observation”, *Magnetic Resonance in Medicine*, vol. 63, no. 2, pp. 385–395, Feb. 2010, ISSN: 07403194. DOI: [10.1002/mrm.22212](https://doi.org/10.1002/mrm.22212). [Online]. Available: <http://doi.wiley.com/10.1002/mrm.22212>.
34. J.-D. Tournier, R. Smith, D. Raffelt, *et al.*, “MRtrix3: A fast, flexible and open software framework for medical image processing and visualisation”, *NeuroImage*, vol. 202, p. 116137, Nov. 2019, ISSN: 10538119. DOI: [10.1016/j.neuroimage.2019.116137](https://doi.org/10.1016/j.neuroimage.2019.116137). [Online]. Available: <https://linkinghub.elsevier.com/retrieve/pii/S1053811919307281>.
35. J. Veraart, E. Fieremans, and D. S. Novikov, “Diffusion MRI noise mapping using random matrix theory”, *Magnetic Resonance in Medicine*, vol. 76, no. 5, pp. 1582–1593, Nov. 2016, ISSN: 07403194. DOI: [10.1002/mrm.23058](https://doi.org/10.1002/mrm.23058). [Online]. Available: <http://doi.wiley.com/10.1002/mrm.23058>.
36. J. Veraart, D. S. Novikov, D. Christiaens, *et al.*, “Denoising of diffusion MRI using random matrix theory”, *NeuroImage*, vol. 142, pp. 394–406, Nov. 2016, ISSN: 1053-8119. DOI: [10.1016/j.neuroimage.2016.08.016](https://doi.org/10.1016/j.neuroimage.2016.08.016). [Online]. Available: <https://www.sciencedirect.com/science/article/pii/S1053811916303949?via%7B%5C%7D3Dihub>.
37. P. J. Basser, J. Mattiello, and D. Lebihan, “Estimation of the Effective Self-Diffusion Tensor from the NMR Spin Echo”, *Journal of Magnetic Resonance, Series B*, vol. 103, no. 3, pp. 247–254, Mar. 1994, ISSN: 10641866. DOI: [10.1006/jmrb.1994.1037](https://doi.org/10.1006/jmrb.1994.1037).
38. J.-D. Tournier, F. Calamante, D. G. Gadian, *et al.*, “Direct estimation of the fiber orientation density function from diffusion-weighted MRI data using spherical deconvolution”, *NeuroImage*, vol. 23, no. 3, pp. 1176–1185, Nov. 2004, ISSN: 1053-8119. DOI: [10.1016/j.neuroimage.2004.07.037](https://doi.org/10.1016/j.neuroimage.2004.07.037). [Online]. Available: <https://www.sciencedirect.com/science/article/pii/S1053811904004100?via%7B%5C%7D3Dihub>.
39. J.-D. Tournier, F. Calamante, and A. Connelly, “Robust determination of the fibre orientation distribution in diffusion MRI: Non-negativity constrained super-resolved spherical deconvolution”, *NeuroImage*, vol. 35, no. 4, pp. 1459–1472, May 2007, ISSN: 1053-8119. DOI: [10.1016/j.neuroimage.2007.02.016](https://doi.org/10.1016/j.neuroimage.2007.02.016). [Online]. Available: <https://www.sciencedirect.com/science/article/pii/S1053811907001243>.
40. N. J. Tustison, B. B. Avants, P. A. Cook, *et al.*, “N4ITK: improved N3 bias correction.”, *IEEE transactions on medical imaging*, vol. 29, no. 6, pp. 1310–20, Jun. 2010, ISSN: 1558-254X. DOI: [10.1109/TMI.2010.2046908](https://doi.org/10.1109/TMI.2010.2046908). [Online]. Available: <http://www.ncbi.nlm.nih.gov/pubmed/20378467%20http://www.pubmedcentral.nih.gov/articlerender.fcgi?artid=PMC3071855>.
41. J.-D. Tournier, F. Calamante, and A. Connelly, “Determination of the appropriate  $\langle b \rangle$  value and number of gradient directions for high-angular-resolution diffusion-weighted imaging”, *NMR in Biomedicine*, vol. 26, no. 12, pp. 1775–1786, Dec. 2013, ISSN: 09523480. DOI: [10.1002/nbm.3017](https://doi.org/10.1002/nbm.3017). [Online]. Available: <http://doi.wiley.com/10.1002/nbm.3017>.
42. D. Raffelt, J.-D. Tournier, S. Crozier, *et al.*, “Reorientation of fiber orientation distributions using apodized point spread functions”, *Magnetic Resonance in Medicine*, vol. 67, no. 3, pp. 844–855, Mar. 2012, ISSN: 07403194. DOI: [10.1002/mrm.23058](https://doi.org/10.1002/mrm.23058). [Online]. Available: <http://doi.wiley.com/10.1002/mrm.23058>.
43. D. Raffelt, J.-D. Tournier, S. Rose, *et al.*, “Apparent Fibre Density: A novel measure for the analysis

- of diffusion-weighted magnetic resonance images”, *NeuroImage*, vol. 59, no. 4, pp. 3976–3994, Feb. 2012, ISSN: 1053-8119. DOI: [10 . 1016 / J . NEUROIMAGE . 2011 . 10 . 045](https://doi.org/10.1016/j.neuroimage.2011.10.045). [Online]. Available: <https://www.sciencedirect.com/science/article/pii/S1053811911012092?via%7B%5C%7D3Dihub>.
44. H. Ouchi, K. Yamada, K. Sakai, *et al.*, “Diffusion anisotropy measurement of brain white matter is affected by voxel size: Underestimation occurs in areas with crossing fibers”, *American Journal of Neuroradiology*, vol. 28, no. 6, pp. 1102–1106, Jun. 2007, ISSN: 01956108. DOI: [10.3174/ajnr.A0488](https://doi.org/10.3174/ajnr.A0488).
45. B. Bender and U. Klose, “The in vivo influence of white matter fiber orientation towards  $B_0$  on  $T2^*$  in the human brain”, *NMR in Biomedicine*, vol. 23, no. 9, pp. 1071–1076, Nov. 2010, ISSN: 09523480. DOI: [10 . 1002 / nbm . 1534](https://doi.org/10.1002/nbm.1534). [Online]. Available: <http://doi.wiley.com/10.1002/nbm.1534>.
46. J. Lee, P. van Gelderen, L. W. Kuo, *et al.*, “ $T2^*$ -based fiber orientation mapping”, *NeuroImage*, vol. 57, no. 1, pp. 225–234, Jul. 2011, ISSN: 10538119. DOI: [10.1016/j.neuroimage.2011.04.026](https://doi.org/10.1016/j.neuroimage.2011.04.026).
47. W. Li, B. Wu, A. V. Avram, *et al.*, “Magnetic susceptibility anisotropy of human brain in vivo and its molecular underpinnings”, *NeuroImage*, vol. 59, no. 3, pp. 2088–2097, Feb. 2012, ISSN: 10538119. DOI: [10.1016/j.neuroimage.2011.10.038](https://doi.org/10.1016/j.neuroimage.2011.10.038).
48. S. H. Oh, Y. B. Kim, Z. H. Cho, *et al.*, “Origin of  $B_0$  orientation dependent  $R2^*$  ( $=1/T2^*$ ) in white matter”, *NeuroImage*, vol. 73, pp. 71–79, Jun. 2013, ISSN: 10538119. DOI: [10.1016/j.neuroimage.2013.01.051](https://doi.org/10.1016/j.neuroimage.2013.01.051).
49. S. Foxley, V. Sampathkumar, V. De Andrade, *et al.*, “Multi-modal imaging of a single mouse brain over five orders of magnitude of resolution”, *NeuroImage*, p. 118250, Jun. 2021, ISSN: 10538119. DOI: [10 . 1016 / j.neuroimage.2021.118250](https://doi.org/10.1016/j.neuroimage.2021.118250). [Online]. Available: [https : / / linkinghub . elsevier . com / retrieve / pii / S1053811921005279](https://linkinghub.elsevier.com/retrieve/pii/S1053811921005279).

## Supporting Information

Table S1: Replicated from Table 1 in Nam et al. [11] Initial values and search ranges of the parameters for the magnitude-fit and complex-fit models.  $S_1 = S(\text{TE}_1)$ .  $\Delta f_{\text{bg},\text{init}} = \frac{\left\{ \sum_{n=1}^{N-1} S_n^* S_{n+1} \right\}}{2\pi\Delta\text{TE}}$ : initial  $\Delta f_{\text{bg}}$  ( $N$  = number of echoes used in fitting).

Both models					
	$A_{\text{my}}$	$A_{\text{ax}}$	$A_{\text{ex}}$	$T_{2,\text{my}}^*$ (ms)	$T_{2,\text{ax}}^*$ (ms)
Initial value	$0.1 \times  S_1 $	$0.6 \times  S_1 $	$0.3 \times  S_1 $	10	64
Lower bound	0	0	0	3	25
Upper bound	$2 \times  S_1 $	$2 \times  S_1 $	$2 \times  S_1 $	25	150
Magnitude fit			Complex fit		
	$\Delta f_{\text{my-ex}}$ (Hz)	$\Delta f_{\text{ax-ex}}$ (Hz)	$\Delta f_{\text{my+bg}}$ (Hz)	$\Delta f_{\text{ax+bg}}$ (Hz)	$\Delta f_{\text{ex+bg}}$ (Hz)
Initial value	5	0	$\Delta f_{\text{bg},\text{init}}$	$\Delta f_{\text{bg},\text{init}}$	$\Delta f_{\text{bg},\text{init}}$
Lower bound	-75	-25	$\Delta f_{\text{bg},\text{init}} - 75$	$\Delta f_{\text{bg},\text{init}} - 25$	$\Delta f_{\text{bg},\text{init}} - 25$
Upper bound	75	25	$\Delta f_{\text{bg},\text{init}} + 75$	$\Delta f_{\text{bg},\text{init}} + 25$	$\Delta f_{\text{bg},\text{init}} + 25$
					$\phi_0$ (rad)

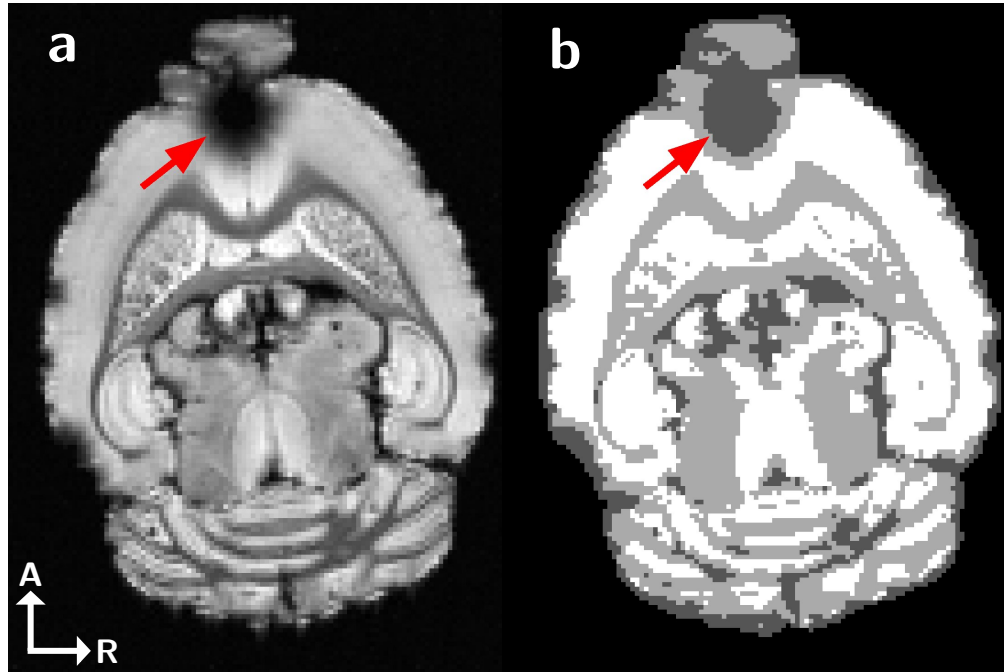


Figure S1: Demonstration of **Atropos** tissue segmentation results. Voxels in the CSF/susceptibility artifact class (dark gray, indicated by red arrow) were excluded from all analysis. A–R axis labels correspond to the Anterior and Right directions, respectively.

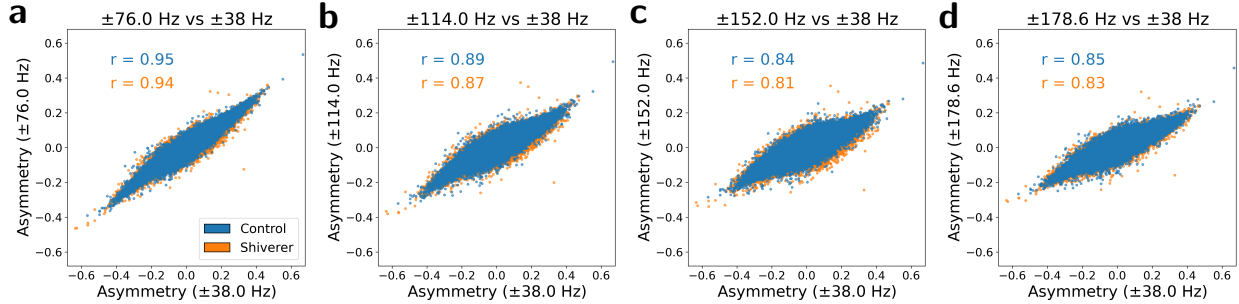


Figure S2: Scatterplots of data-derived asymmetry values calculated with a cutoff frequency of  $\pm 38$  Hz vs. (a)  $\pm 76$  Hz, (b)  $\pm 114$  Hz, (c)  $\pm 152$  Hz, and (d)  $\pm 178.6$  Hz. r-values indicate Pearson's correlation coefficients, which remain above 0.8 for both control and shiverer datasets out to  $\pm 178.6$  Hz.

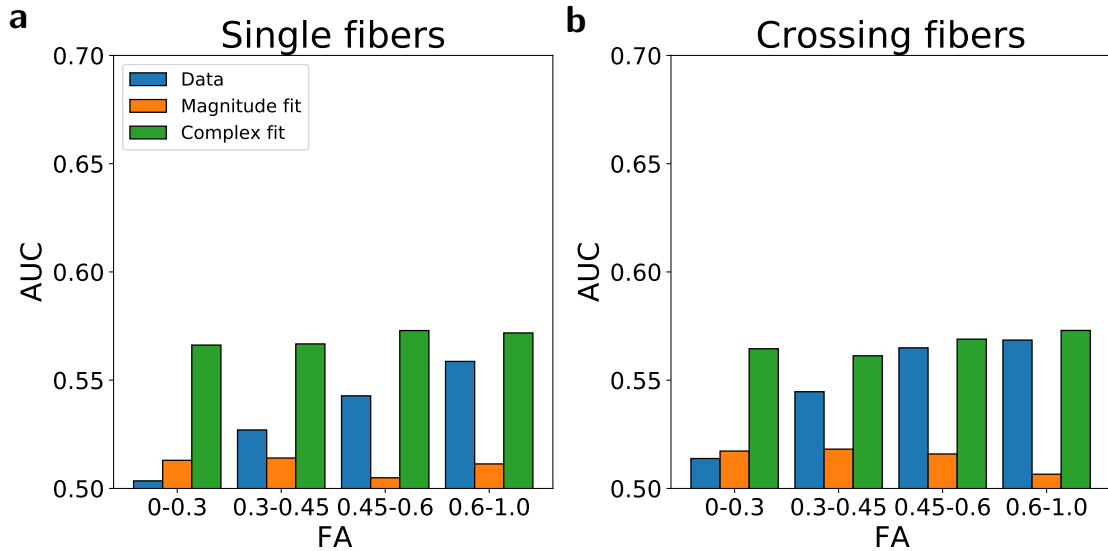


Figure S3: Values for the area under the ROC curve (AUC) using asymmetry as a one-variable classifier for control vs. shiverer data. FIDs were first truncated to 32 echoes prior to model-fitting and calculation of spectral asymmetry. Values represent AUCs for subsets of voxels in different FA bins containing either (a) single or (b) crossing fiber populations. With 32 echoes, neither the data nor either of the models is able to demonstrate meaningful sensitivity to myelin from the asymmetry, highlighting the need for high spectral resolution, or equivalently, extended FID sampling.

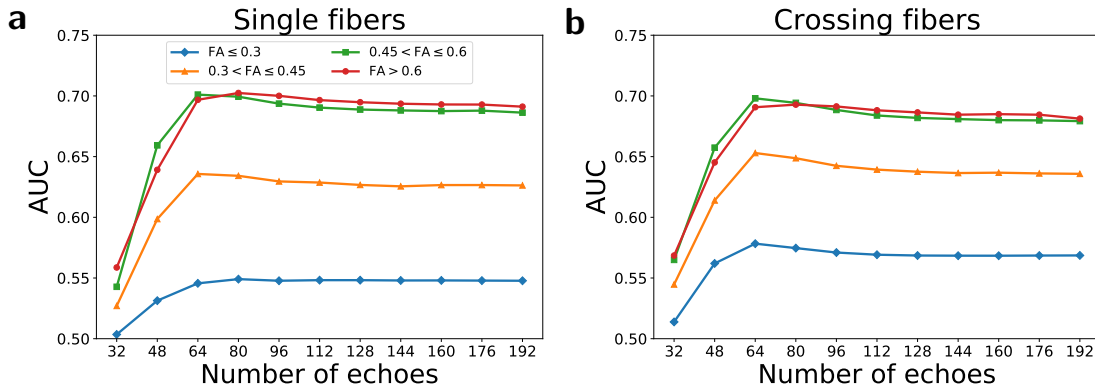


Figure S4: AUC values using data-derived asymmetry as a one-variable classifier for control vs. shiverer data as a function of the number of echoes in the FID. Subsampled-FIDs were created by truncating the full (192 echo) FIDs to the specified values prior to calculating asymmetry in the frequency domain. Values represent AUCs for subsets of voxels in different FA bins containing either (a) single or (b) crossing fiber populations. This demonstrates the importance of spectral resolution, or equivalently, extended FID sampling, and provides a roadmap for future benchmarking studies using EPSI spectral data.